

Inverse Rare-Earth Perovskites of Main-Group Metals – Evolution of Properties and Chemical Bonding

Martin Kirchner, Frank Gäbler, Walter Schnelle, Frank R. Wagner, and Rainer Niewa¹

Inverse Perovskites of the general composition $((A,R)_3Z)E$ consisting of alkaline-earth metals (A) or rare-earth metals (R), nonmetals ($Z = C, N, O$) and main group elements of the p -block (E) can be varied in the chemical composition in an extremely wide range within one adherent crystal structure type. The compounds cover semiconductors as well as electron excess and deficient metals. For these reasons, inverse Perovskites provide ideal systems to study chemical and physical properties depending on the constituents with focus on electronic and magnetic behavior as well as interdependencies of chemical bonding.

In binary systems of rare-earth metals and main-group metals, compounds with the composition R_3E that crystallize in the hexagonal Mg_3Cd structure and a cubic Cu_3Au type modification are frequently reported. In particular, Cu_3Au type phases were often investigated, sometimes with controversial results. The reason appears to be the presence of ternary compounds involving unnoticed nonmetallic constituents as, e.g., oxygen. For the systems considered, the phases R_3E with cubic Cu_3Au structure type show the same metal substructure as cubic Perovskites $(R_3Z)E$ ($Z = O, N, C$). Differences in X-ray powder diffraction (XRD) intensities are only marginal, just the unit cell parameters may vary slightly on introduction of nonmetallic components Z . The introduction of Z may lead to compounds with small homogeneity ranges and compositions close to $(R_3Z)E$ or, alternatively, to phases with large homogeneity ranges in the sense of $(R_3Z_x)E$ depending on element combinations and particularly on the chemical nature of Z . Physical (e.g., magnetic and mechanical), chemical and bonding properties strongly depend on element combination and composition of the phase. Here we discuss these influences exemplarily for the systems $(La_3Z_x)Al$ and $(Ce_3Z_x)Al$ ($Z = C, N, O$), $(Eu_3O)E$ ($E = In, Sn$) and $(R_3N)Sn$ ($R = La - Sm$). These investigations continue a study on the rare-earth metal nitrides of indium $(R_3N)In$ as discussed in detail in a previous scientific report [1] and a recent publication [2].

In the binary systems $R-Al$ phases with the composition R_3Al were reported for $R = Y, La - Nd, Sm$ [3-8]. La_3Al was found to exist only in the small temperature window of $670 K < T < 790 K$ with the hexagonal Mg_3Cd structure [4]. Several reports suggest a cubic La_3Al high-temperature polymorph [9, 10]. According to the majority of phase diagrams available, the binary compound Ce_3Al crystallizes in the hexagonal Mg_3Cd structure type at ambient temperature and transforms to a cubic Cu_3Au type modification above $T = 520 K$. However, there are observations that quenched melt beads of the Ce containing system exclusively consisted of hexagonal $\alpha-Ce_3Al$, while a transformation into a cubic phase on annealing in quartz ampoules [11] or MgO crucibles [12] was apparent. In the binary systems $R-Sn$ phases R_3Sn were previously confirmed only for $R = La, Ce, Pr$. All three compounds were described to crystallize in the Cu_3Au structure type [13, 14]. La_3Sn is under discussion since it does not appear in any phase diagram, but is reported to show superconductivity below $T_c = 6.2 K$ [15]. In the binary systems $Eu-In$ and $Eu-Sn$ no compounds with the composition Eu_3E are known.

For $Z = C$ a huge variety of rare-earth metal compounds $(R_3C)E$ was reported in the past about fifty years [16]. All such rare-earth metal carbides are expected to be brittle and to show considerable electric conductivity. Remarkably, the respective europium containing carbides and corresponding alkaline-earth metal carbides are not known. Nitrides with metallic properties were reported for $E = Al, Ga, In, Tl, Sn, Pb$ in combination with a large variety of trivalent rare-earth metals [2, 8, 17, 18, 19]. Respective Yb and Eu containing nitrides are unknown so far. Such nitrides may exist in analogy to the alkaline-earth metal nitrides [20 - 23]. Interestingly, only few inverse Perovskite oxides of the rare-earth metals have been reported: metallic $(La_3O)In$ [19], $(La_3O)Al$, $(Ce_3O)Al$ [17], and $(R_3O)E(14)$ ($R = Eu, Yb, E(14) = \text{group 14 element}$) [24, 25].

Systems $(R_3Z)Al$ ($R = La, Ce; Z = O, N, C$)

Formation and Crystal Structures

Preparation of the ternary phases $(R_3Z)Al$ (specifically with $R = La, Ce$) can be carried out as previously described for the analogous In containing phases [2]. A general difference of the Al containing systems compared to those with In is the higher thermal stability of the metal-rich nitrides and the tendency for formation of ternary nitridoaluminates. The high thermal stability, even against reaction with nitrogen, can be seen from the fact, that La–Al melt beads react with nitrogen to form $(La_3N)Al$ as main product at temperatures in the range of $1070\text{ K} < T < 1270\text{ K}$. According to our experiments $(La_3N)Al$ is probably the kinetically favored product when treated under excess nitrogen gas because the amount decreases with increased reaction duration in favor of the binary metal nitrides LaN and AlN. Corresponding phases in the systems R –In either do not react with nitrogen under these conditions (but at higher temperatures), or form RN and In in a rapid reaction [2, 26]. Preparation of oxides, for comparison, was achieved from oxide precursors, while excess oxygen leads to aluminate products. Experiments aiming for ‘ $(Ce_3C)Al$ ’ led to samples containing the cubic Perovskite next to unknown phases. On reduction of the carbon amount at a total composition of $(Ce_3C_x)Al$ with $x \approx 0.65$, the highest amount of the cubic Perovskite in a multiphase sample was obtained, while on further reduction of the carbon content hexagonal α - Ce_3Al is in equilibrium with the Perovskite carbide.

XRD performed on the ternary compounds $(R_3Z)Al$ ($R = La, Ce; Z = O, N, C$) clearly indicate the Cu_3Au type metal substructure. Refinement results of X-ray diffraction intensity data taken on a single crystal $(La_3N)Al$ support the structural assignment and reveal the nitride ions to be located in octahedral holes exclusively formed by La, i.e., a cubic Perovskite type structure. The obtained data give no indication for a significant homogeneity range of this ternary compound. Anisotropic refinements of the displacement parameters of La led to strongly oblate ellipsoids orientated perpendicular to the N–La direction. Such a displacement was frequently observed for related binary octahedral framework structures with ReO_3 structure type (e.g., Cu_3N [27] and ReO_3 itself [28, 29]) as well as a variety of Perovskites ABO_3 . It was often associ-

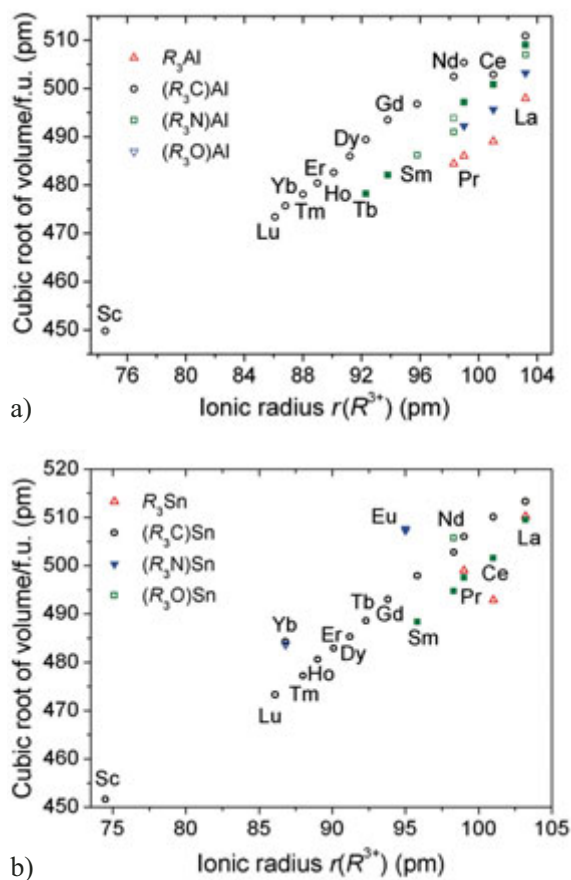


Fig. 1. Cubic root of the volumes per formula unit $(V_0)^{1/3}$ for compounds a) $(R_3Z)Al$ b) $(R_3Z)Sn$ with $Z = \square, C, N, O$ as a function of the radii of the rare-earth metal ions $r(R^{3+})$ ($CN = 6$), full symbols: own values, open symbols: data taken from literature.

ated with atomic/ionic size mismatch in the structure prior distortion. For comparison, the closely related cubic Perovskite nitride $(Ca_3N)Ti$ exhibits nearly no anisotropy of Ca [23], indicating a perfect size fit, while, e.g., the nitrides $(Ca_3N)E$ with $E = P, As$ [20, 30] and the oxides $(A_3O)E$ with $A = Ca, Sr, Ba$ and $E = Si, Ge$ [24, 25, 31] are distorted to orthorhombic unit cells (space group $Pnma$).

The unit cell volumes of the carbides are significantly larger than those of the nitrides, oxides, and particularly the binary (hexagonal) phases. The reported unit cell of $(Ce_3C)Al$ [16, 32] deviates to lower values than expected from those of the oxide and nitride and nearly coincides with that of $(Ce_3N)Al$ (Fig. 1a). This observation was discussed to arise from a $Ce^{4+}(4f^0)$ contribution in the carbide [16], while the volumes of the nitride and oxide are

consistent with an exclusive $\text{Ce}^{3+}(4f^1)$ content. The reported unit cell parameters for $(\text{Ce}_3\text{C})\text{Al}$ were in principle reproduced in the present work, but on a sample of the solid solution series $(\text{Ce}_3\text{C}_{1-x}\text{N}_x)\text{Al}$ ($(\text{Ce}_3\text{C}_{0.82(2)}\text{N}_{0.12(2)})\text{Al}$ according to chemical analyses). Data on samples with various carbon contents of bulk compositions ' $(\text{Ce}_3\text{C}_x)\text{Al}$ ' indicate a compound with an approximate composition parameter $x = 0.65$ (see above).

Magnetization measurements on single phase samples $(\text{Ce}_3\text{C}_{1-x}\text{N}_x)\text{Al}$ ($x = 0.15$) are consistent with Ce in a pure $\text{Ce}^{3+}(4f^1)$ state (see below), thus leaving substitution on the C site by N and/or O as the most likely reason for the smaller unit cell dimension also for the literature data. Similarly, phase analyses in the systems Ce–Al–N and Ce–Al–O led to the conclusion that $(\text{Ce}_3\text{N})\text{Al}$ and $(\text{Ce}_3\text{O})\text{Al}$ tolerate only small deficiencies x on the Z site in the sense of $(\text{Ce}_3\text{Z}_{1-x})\text{Al}$. In samples with $Z = \text{N}, \text{O}$ contents below the nominal amount for the formation of $(\text{Ce}_3\text{Z})\text{Al}$ always hexagonal Ce_3Al was observed as a second phase as is illustrated in Figure 2: DTA measurements on samples with the bulk compositions $(\text{Ce}_3\text{N}_x)\text{Al}$ and $x = 0.2, 0.4, 0.6, 0.8, 1$, annealed at $T = 870$ K and subsequently quenched to ambient temperature are shown. The respective XRD patterns taken prior to the thermal analyses (Fig. 2) indicate that hexagonal $\alpha\text{-Ce}_3\text{Al}$ is present in all samples with $x < 1$, while the sample with $x = 1$ ($(\text{Ce}_3\text{N}_{1.01(1)})\text{Al}$ according to chemical analyses) gives a diagram fully explained by a cubic Perovskite structure. Qualitatively, the amount of

hexagonal $\alpha\text{-Ce}_3\text{Al}$ decreases with increasing x , while the amount of $(\text{Ce}_3\text{N})\text{Al}$ increases. The relatively weak intensities of the reflections caused by $\alpha\text{-Ce}_3\text{Al}$ compared to those from the ternary Perovskite nitride are due to the mechanical properties of both phases: the binary compound is ductile while the ternary nitride is brittle. Therefore, the microcrystalline powder is enriched in nitride crystallites of suitable size after grinding. Corresponding to these XRD patterns, the DTA curves reveal endothermal signals at $T_{\text{max}} = 925$ K, which represent melting of Ce_3Al . The size of this peak decreases with increasing x conversely to a growing endothermal signal at $T_{\text{max}} = 1340$ K. The XRD patterns of the samples after the thermal analyses show no significant differences to those recorded before the DTA and the sample with $x = 1$ was clearly molten. The DTA signal at $T_{\text{max}} = 1340$ K is thus interpreted as congruent melting point of $(\text{Ce}_3\text{N})\text{Al}$, which exhibits no significant homogeneity range $(\text{Ce}_3\text{N}_x)\text{Al}$ within the $\Delta x = 0.2$ step frame of the experiments. A small systematic variation of the DTA peak temperatures may indicate the possibility of a small N deficiency, but is favorably connected with the progression of the liquidus. Similar DTA and XRD investigations for the quasi-binary systems $\text{Ce}_3\text{Al}-(\text{Ce}_3\text{O})\text{Al}$ indicate also small homogeneity ranges for both Ce_3Al and $(\text{Ce}_3\text{O})\text{Al}$. In addition, the experiments revealed large homogeneity ranges in the sense of substitution of C and O by N in the ternary carbide and oxide, respectively, i.e., $(\text{Ce}_3\text{C}_{1-x}\text{N}_x)\text{Al}$ and $(\text{Ce}_3\text{O}_{1-x}\text{N}_x)\text{Al}$.

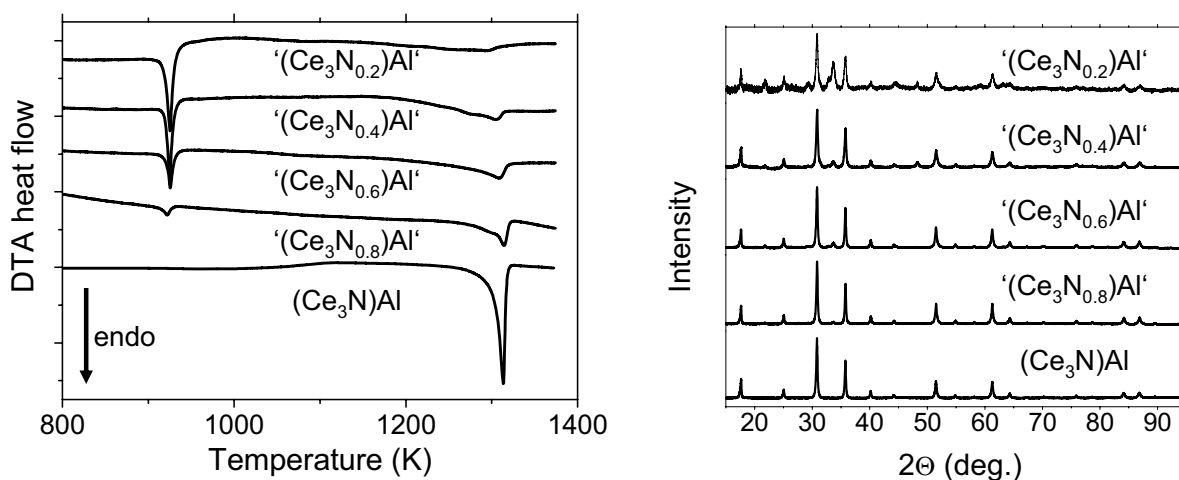


Fig. 2. DTA measurements (left) and XRD patterns (right) on samples of the bulk compositions ' $(\text{Ce}_3\text{N}_x)\text{Al}$ ' with $x = 0.2, 0.4, 0.6, 0.8, 1$. The XRD patterns depicted were taken prior the DTA measurements, showing reflection profiles of hexagonal $\alpha\text{-Ce}_3\text{Al}$ decreasing with increasing N content, and of $(\text{Ce}_3\text{N})\text{Al}$ increasing with increasing N content.

Within this study, experiments aiming for cubic β - Ce_3Al always resulted in the hexagonal phase. There are likewise no indications for a transition of hexagonal α - Ce_3Al into a high-temperature polymorph (β - Ce_3Al with Cu_3Au structure type as was reported in literature [11, 12]) from thermal analyses as discussed above. This observation is in line with the report that α - Ce_3Al does not show any discontinuity or aberration in the magnetic susceptibility at the presumed transition temperature to β - Ce_3Al [12]. This result indicates that the previous observations of cubic β - Ce_3Al may be due to the presence of nonmetal-stabilized ternary phases.

Magnetic and Electronic Properties

Data of the magnetic susceptibility of $(\text{Ce}_3\text{O})\text{Al}$, $(\text{Ce}_3\text{N})\text{Al}$, and $(\text{Ce}_3\text{C}_{1-x}\text{N}_x)\text{Al}$ ($x = 0.15$) are given in Figure 3. The curvature of $1/\chi(T)$ at temperatures below 100 K and the almost linear variation of all three data sets at high temperatures indicate the presence of the $^2F_{5/2}$ crystal field ground multiplet of the $4f^1$ electronic configuration of Ce.

$(\text{Ce}_3\text{O})\text{Al}$ orders antiferromagnetically at $T_N = 9(1)$ K, $(\text{Ce}_3\text{N})\text{Al}$ at $T_N = 6(1)$ K, while $(\text{Ce}_3\text{C}_{1-x}\text{N}_x)\text{Al}$ ($x = 0.15$) shows no indication for a magnetic order down to $T = 2$ K. These transition temperatures decrease with increasing unit cell parameters and thus with increasing distances $d(\text{Ce}-\text{Ce})$. Similar to $(\text{Ce}_3\text{C}_{1-x}\text{N}_x)\text{Al}$ ($x = 0.15$), hexagonal α - Ce_3Al (and ‘cubic Ce_3Al ’) is known to show no magnetic order above $T = 4$ K and an effective magnetic moment of $\mu_{\text{eff}}/\text{Ce-atom} = 2.52 \mu_B$ at high temperatures [12].

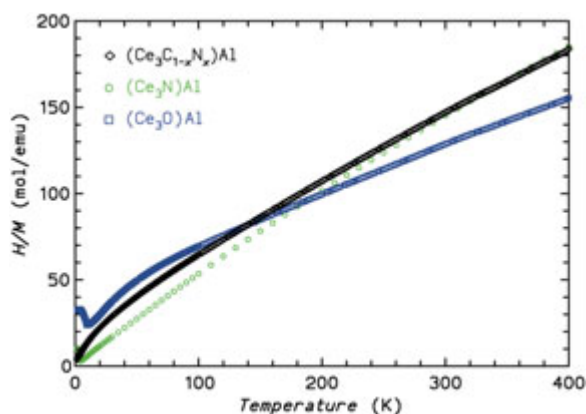


Fig. 3. Inverse magnetic susceptibility of $(\text{Ce}_3\text{C}_{1-x}\text{N}_x)\text{Al}$ (black diamonds, $x = 0.15$, no apparent magnetic order above $T = 2$ K), $(\text{Ce}_3\text{N})\text{Al}$ (green circles, $T_N = 6$ K) and $(\text{Ce}_3\text{O})\text{Al}$ (blue squares, $T_N = 9$ K) measured in an external field of $\mu_0H = 1$ T as a function of temperature.

Measurements of the heat capacity on $(\text{Ce}_3\text{C}_{1-x}\text{N}_x)\text{Al}$ ($x = 0.15$) down to temperatures of 1.8 K show no phase transitions but a steep increase in c_p/T below 4.5 K. Since $\text{Ce}^{3+}(4f^1)$ is a Kramers ion, where the minimum degeneracy is that of a doublet, application of a magnetic field leads to a splitting of the crystal field ground state. Therefore, a distorted two-level Schottky anomaly develops with increasing field (Fig. 4). The entropy contained in the Schottky anomaly is around $k_B N_A \ln 2$, thus confirming that the ground state is a doublet. Only measurements at lower temperatures can clarify whether the upturn ($\propto T^{-2}$) in zero field indicates a magnetic ordering in the ground state doublet (of which the short-range order tail is seen in zero field). The energy splitting of the ground doublet necessary to reproduce the upturn in c_p/T below 4.5 K is well below $k_B \times 1$ K. Subtraction of a Debye lattice term (Debye temperature 250 K) produces a large multi-level Schottky anomaly with a maximum of $\approx 20 \text{ J mol}^{-1} \text{ K}^{-1}$ height at ≈ 31 K. A crystal field level scheme with the doublet ground state and a quasi-quartet excited state at $k_B \times 83$ K (two doublets near that energy) nicely reproduces this Schottky anomaly.

The sample $(\text{La}_3\text{N})\text{Al}$ displayed Pauli paramagnetism ($\chi_P \approx +160 \times 10^{-6} \text{ emu mol}^{-1}$) in the investigated temperature range. The derived value of χ_P corresponds to an electronic density of states of $\approx 5 \text{ states eV}^{-1}$ at E_F which has to be compared with 2.9 states eV^{-1} found in electronic structure calculations discussed below (*vide infra*).

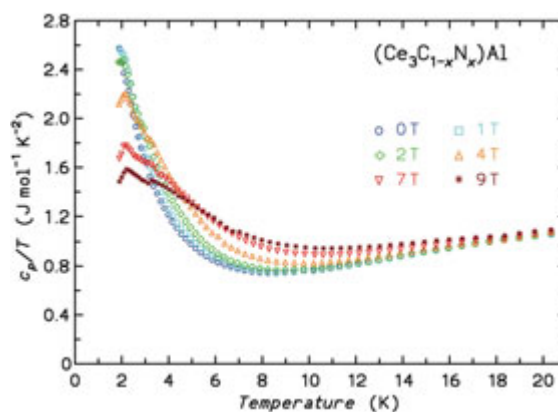


Fig. 4. $(\text{Ce}_3\text{C}_{1-x}\text{N}_x)\text{Al}$ ($x = 0.15$): c_p/T in different external magnetic fields vs. temperature. Circles: zero external field, squares: $\mu_0H = 1$ T, diamonds: $\mu_0H = 2$ T, triangles up: $\mu_0H = 4$ T, triangles down: $\mu_0H = 7$ T, asterisks: $\mu_0H = 9$ T.

For independent information on the electronic state of cerium we measured XAS at the Ce- L_{III} threshold. Figure 5 shows the Ce- L_{III} edge of $(\text{Ce}_3\text{O})\text{Al}$, $(\text{Ce}_3\text{N})\text{Al}$ and $(\text{Ce}_3\text{C}_{1-x}\text{N}_x)\text{Al}$ together with the spectrum of CeO_2 as a reference. No indication for a $\text{Ce}^{4+}(4f^0)$ contribution at increased energies is visible for compounds $(\text{Ce}_3\text{Z})\text{Al}$, which is consistent with a $\text{Ce}^{3+}(4f^1)$ state throughout. Additionally shown is the spectrum of the sample ‘ $(\text{Ce}_3\text{C}_{0.7})\text{Al}$ ’ with the highest carbon content of a cubic Perovskite compound in a carbide sample, as stated above. The occurrence of exclusively $\text{Ce}^{3+}(4f^1)$ contributions to the spectrum indicates that the reported small volume of ‘ $(\text{Ce}_3\text{C})\text{Al}$ ’ is not caused by an increased valence state of Ce, but is due to a C deficiency.

The electrical resistivity $\rho(T)$ of $(\text{Ce}_3\text{N})\text{Al}$ amounts to $\rho(300\text{ K}) \approx 1\ \mu\Omega\text{m}$ at 300 K and decreases linearly with decreasing temperature indicating metallic conductivity. No clear discontinuity is visible around T_N as can be expected from the small deGennes factor of $\text{Ce}^{3+}(4f^1)$. The resistivity of $(\text{Ce}_3\text{C}_{1-x}\text{N}_x)\text{Al}$ ($x = 0.15$) is considerably larger ($\rho(300\text{ K}) \approx 2.4\ \mu\Omega\text{m}$) and decreases non-linearly and with little temperature dependence down to about $T = 50\text{ K}$. Below this temperature

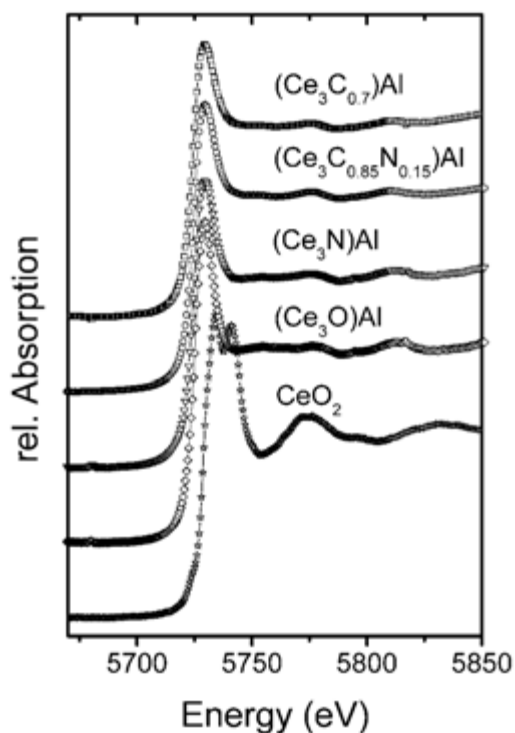


Fig. 5. XAS spectra at the Ce- L_{III} edge of $(\text{Ce}_3\text{O})\text{Al}$, $(\text{Ce}_3\text{N})\text{Al}$, $(\text{Ce}_3\text{C}_{0.85}\text{N}_{0.15})\text{Al}$, $(\text{Ce}_3\text{C}_{0.7})\text{Al}$ and CeO_2 for energy reference.

$\rho(T)$ increases again. Together with the absence of magnetic order above 1.8 K (in $\chi_0 H = 10\text{ mT}$) and the heat capacity data, the temperature dependence of the electrical resistivity leads us to conclude on some kind of frustration of magnetic exchange due to disorder. Competing ferromagnetic and antiferromagnetic interactions could be induced by slightly different distances $d(\text{Ce}-\text{Ce})$ due to disorder in the C, N sublattice. Structural disorder may also explain the large absolute resistivity of this material. The electrical resistivity of $(\text{La}_3\text{Al})\text{N}$ is $0.67\ \mu\Omega\text{m}$ at 300 K, typical for metals.

Band Structure Calculations and Chemical Bonding

In order to elucidate some principle features and trends of the electronic structures we performed scalar relativistic LDA band structure calculations. For reasons of simplicity we restricted these to the lanthanum compounds $(\text{La}_3\text{O})\text{Al}$, $(\text{La}_3\text{N})\text{Al}$, and $(\text{La}_3\text{C})\text{Al}$ using experimental lattice parameters.

From analyses of the densities of states (DOS) of the valence bands (Fig. 6, $Z(2s)$ bands omitted in the discussion due to low energy positions) it is evident that they cannot simply be interrelated by the frozen band approximation. This is mainly due to the different energetic positions and energy bandwidths of the $Z(2p)$ bands. The energy of the bands increases with respect to E_F according to $E(\text{O}(2p)) < E(\text{N}(2p)) < E(\text{C}(2p))$, which is the common trend expected from the first atomic ionization potentials, atomic electronegativities and atomic charge dependence of band positions. The $2p$ bandwidth increases along O to C, which is caused by mixing with $\text{La}(5d)$ minority band states forming partially covalent bonds (see below). While for $Z = \text{O}, \text{N}$ the $2p$ bands are lying well below E_F , the combined effects of increasing energetic position and bandwidth lead for $(\text{La}_3\text{C})\text{Al}$, to a situation with the $\text{C}(2p)$ band closely below the Fermi level with even some contributions at E_F .

The $\text{Al}(3s)$ band can be characterized to a good approximation as a pure $3s$ band, which remains at roughly the same energy position well below E_F for all three compounds considered. The seemingly strong differences in the DOS diagrams result from the fact that the broader $Z(2p)$ band DOS contributions are overlapping in energy with narrower $\text{Al}(3s)$ band contributions, partly for $(\text{La}_3\text{O})\text{Al}$, and completely for $(\text{La}_3\text{N})\text{Al}$, while for $Z = \text{C}$ they are located clearly above the $\text{Al}(3s)$ band.

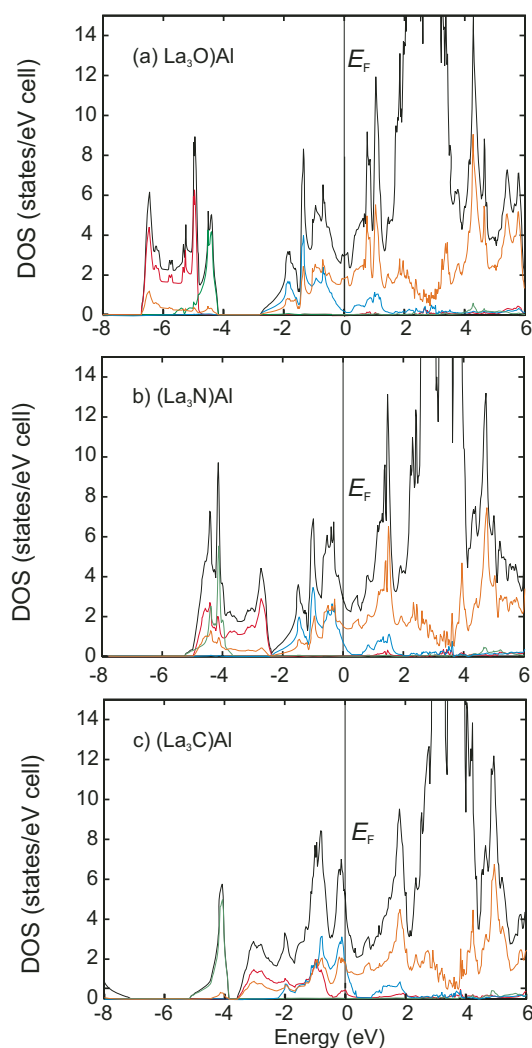


Fig. 6. Total DOS and local DOS projections for a) $(\text{La}_3\text{O})\text{Al}$, b) $(\text{La}_3\text{N})\text{Al}$ and c) $(\text{La}_3\text{C})\text{Al}$. Color code: Total DOS black, $Z(2p)$ red, $\text{Al}(3s)$ green, $\text{Al}(3p)$ blue, $\text{La}(5d)$ orange.

$\text{Al}(3p)$ bands are located in the upper energy region roughly between -3 eV and $+2$ eV, where they are strongly mixed with $\text{La}(5d)$ contributions. The energies of filled $\text{Al}(3p)$ bands mark the region where metal–metal bonding takes place. Exclusively for $(\text{La}_3\text{C})\text{Al}$ this region partially overlaps with the energy region of $Z(2p)$ bands, and, in contrast to $Z = \text{O}, \text{N}$, result in a DOS contribution of $Z(2p)$ at E_F .

The total DOS at E_F represents 3.0 states/eV ($Z = \text{O}$), 2.9 states/eV ($Z = \text{N}$) and 4.9 states/eV ($Z = \text{C}$). The significantly larger value for $Z = \text{C}$ is due to the position of E_F located on the falling flank of a DOS peak, while E_F lies between this and the next higher energy peak for $Z = \text{O}, \text{N}$. This difference is directly related to the fewer number of

valence electrons for $(\text{La}_3\text{C})\text{Al}$ compared to the compounds with O and N. Therefore, the number of states at the Fermi level can chemically be tailored by formation of substitution phases according to, e.g., $(\text{La}_3\text{C}_{1-x}\text{N}_x)\text{Al}$.

In order to further characterize chemical bonding within this local DOS picture we calculated energy-resolved Crystal Orbital Hamiltonian Populations (COHP) indicating three significant interatomic two-center orbital interactions (Fig. 7): COHP($Z(2p)$ – $\text{La}(5d)$) diagrams corroborate the picture of partially covalent bonding between elements Z and La, where the strength of orbital interactions increases from O to C explaining the emerging $Z(2p)$ dispersion. Orbital interactions Z –La are clearly optimized in the sense that all available bonding contributions are exhausted either well below E_F for $Z = \text{O}, \text{N}$, or just at E_F for $Z = \text{C}$, and only neglectable antibonding contributions occur for $Z = \text{N}, \text{O}$.

In the projected DOS for $\text{Al}(3p)$ a pseudo gap occurs close to E_F which is covered in the total DOS by large $\text{La}(5d)$ contributions. This splitting of $\text{Al}(3p)$ states is caused by $\text{Al}(3p)$ – $\text{La}(5d)$ orbital interactions, which give bonding contributions below and antibonding contributions above the pseudo gap (Fig. 7). For $(\text{La}_3\text{O})\text{Al}$ the Fermi level lies within that pseudo gap, so that orbital interactions Al –La are optimized in the sense of separating bonding from antibonding contributions by the Fermi level. Already starting for $Z = \text{N}$, but especially for $(\text{La}_3\text{C})\text{Al}$, E_F increasingly cuts the falling flank of the partial $\text{Al}(3p)$ DOS below the pseudo gap and thus, increasingly significant bonding contributions are lost (located above E_F). This is not compensated by a corresponding gain of competing bonding interactions. It has been discussed previously for isostructural $(\text{La}_3\text{N})\text{In}$ [2] that these heteroatomic intermetallic interactions play an important role for the electronic structure of the compound since they are sizeable and numerous (each Al atom has 12 La neighbors). The electronic structures of $(\text{La}_3\text{N})\text{In}$ and $(\text{La}_3\text{N})\text{Al}$ are very similar and the conclusions derived for the former compound are valid for the latter as well.

Homoatomic two-center metal orbital interactions are significant only for La. As may be expected, they are far from being exhausted at E_F and increase well beyond. The occurrence of sizeable and similar interactions COHP(La–La) for all three compounds is the puzzling feature that challenges sim-

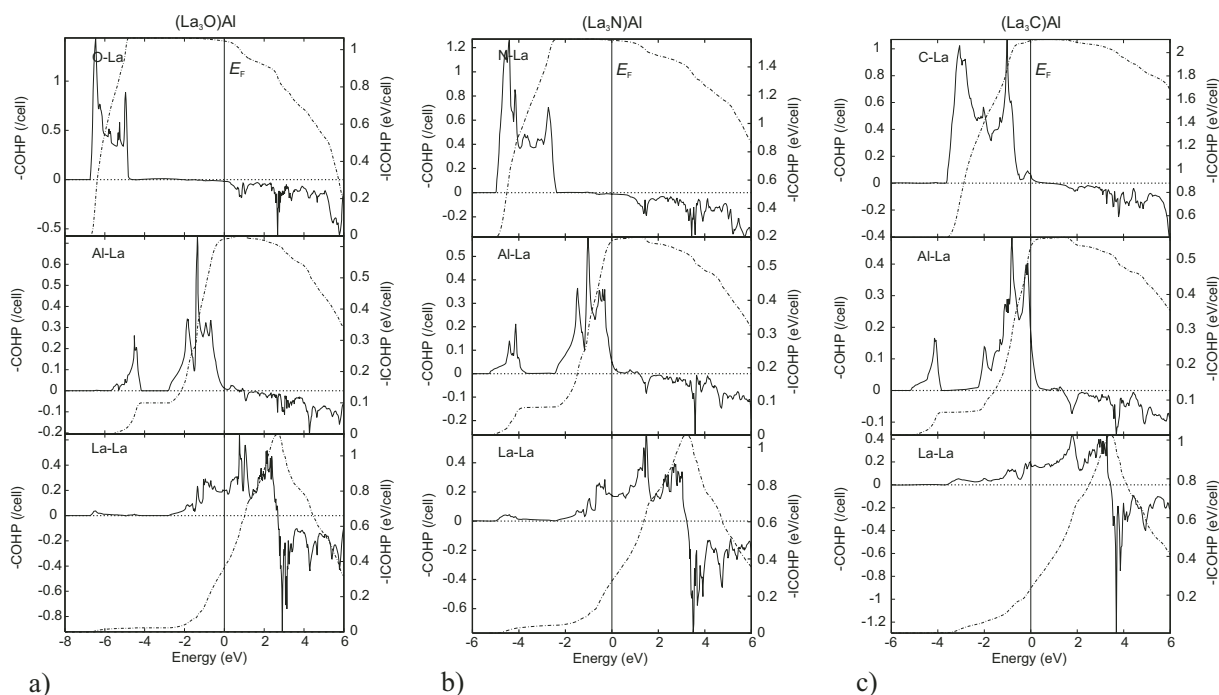


Fig. 7. COHP(E) diagrams of selected interatomic interactions for a) $(\text{La}_3\text{O})\text{Al}$, b) $(\text{La}_3\text{N})\text{Al}$ and c) $(\text{La}_3\text{C})\text{Al}$. Dash-dotted line refers to ordinate axis on the right side and represents the integrated COHP curve (ICOHP).

ple formal charge assignment efforts. The electronic structure of $(\text{La}_3\text{C})\text{Al}$ is to be contrasted with isostructural and — at first glance — isoelectronic $(\text{Ca}_3\text{N})\text{Bi}$ [23]. In the latter case, a formal charge assignment was justified by (i) the absence of sizeable interactions COHP(Ca–Ca) for formal Ca^{2+} species, (ii) the optimization of N–Ca net orbital interactions in the picture of a partial covalent bonding according to $\text{N}^{3-}\text{Ca}^{2+}$, (iii) the optimization of Bi–Ca net orbital interactions (neglecting Bi($6d$) contributions), and (iv) the characteristic compensation of bonding and antibonding contributions below E_F for formal Bi^{3-} species. This way of electron counting within the framework of semiconductor bonding covered by the $(8 - N)$ rule is experimentally corroborated by the existence of an electronic band gap [20]. The only common features of the electronic structures of $(\text{Ca}_3\text{N})\text{Bi}$ and $(\text{La}_3\text{C})\text{Al}$ are the optimization of N–Ca and C–La bonding and the characteristic compensation of bonding and antibonding contributions COHP(Bi–Bi) and COHP(Al–Al), respectively. The occurrence of significant contributions COHP(La–La) below E_F already rules out semiconducting properties for $(\text{La}_3\text{C})\text{Al}$ and the observed electronic conductivities of the various compounds fit these expectations. The reason for the significant and conceptually important electronic La popula-

tion for $(\text{La}_3\text{C})\text{Al}$ are large covalent bonding contributions C–La and Al–La caused by similar orbital energies. It becomes evident that a formal charge assignment $(\text{La}^{3+})_3\text{C}^{4-}\text{Al}^{5-}$ would be in contradiction with the electronic structure. At most, formal charge assignments $(\text{La}_3\text{Al})^{2+}\text{O}^{2-}$, $(\text{La}_3\text{Al})^{3+}\text{N}^{3-}$, and $(\text{La}_3\text{Al})^{4+}\text{C}^{4-}$ can be justified, where — due to the electronic octet situation for species Z — the successive electronic depopulation of the metal substructure becomes evident along O to C. A way to compensate a corresponding loss of metal–metal bonding interactions is the creation of point defects on the Z site, in particular for the carbide. Thus, e.g., a 25 atom% C-deficient $(\text{La}_3\text{C}_{0.75})\text{Al}$ would have to be written according to $(\text{La}_3\text{Al})^{3+}(\text{C}^{4-})_{0.75}$, i.e., the electronic situation for metal–metal bonding is expected to be closely related to the nitride compound.

Systems $(\text{Eu}_3\text{O})E$ ($E = \text{In}, \text{Sn}$)

Formation and Crystal Structures

Compounds $(\text{Eu}_3\text{O})E$ ($E = \text{In}, \text{Sn}$) also crystallize as inverse Perovskites [39]. A single crystal structure refinement on $(\text{Eu}_3\text{O})\text{In}$ points towards a full occupancy of the O site. However, chemical analyses for the sample used for physical properties

measurements resulted in a composition $(\text{Eu}_3\text{N}_{0.030(6)}\text{O}_{0.76(6)})\text{In}$. These data may indicate a homogeneity range in the sense of oxygen deficiency. Anisotropic refinements of the displacement parameters of Eu revealed oblate ellipsoids perpendicular to the O–Eu direction.

The unit cell dimension of $(\text{Eu}_3\text{O})\text{Sn}$ deviates from the simple lanthanide contraction (Fig. 1b) observed for the other rare-earth metal compounds to a similar extent as the respective In compound [1, 2]. This indicates the presence of $\text{Eu}^{2+}(4f^7)$ rather than $\text{Eu}^{3+}(4f^6)$ as will be demonstrated below. The size of the unit cell of $(\text{Yb}_3\text{C})\text{Sn}$ clearly deviates from the monotonic behavior to a larger value [19], which might be interpreted as an indication for a $\text{Yb}^{2+}(4f^{14})$ contribution. This view is supported by data on $(\text{Yb}_3\text{O})\text{Sn}$ [24], where the cubic unit cell parameter indicates the presence of $\text{Yb}^{2+}(4f^{14})$. Except for $(\text{Yb}_3\text{O})\text{Sn}$ the only oxide reported so far is $(\text{Eu}_3\text{O})\text{Sn}$ [25]. The obtained cubic unit cell parameter of $(\text{Eu}_3\text{O})\text{Sn}$ corresponds well with this literature value.

Magnetic and Electronic Properties

The inverse magnetic susceptibilities $1/\chi = H/M$ of $(\text{Eu}_3\text{O})\text{In}$ and $(\text{Eu}_3\text{O})\text{Sn}$ are displayed in Figure 8. At high temperatures both are Curie-Weiss paramagnets with the $^8S_{7/2}$ ground state multiplet of the $4f^7$ configuration of Eu^{2+} . The Eu^{2+} ions in the In compound order ferromagnetically at 185(5) K while those in the Sn compound actually order antiferromagnetically at 31.4(2) K (inset Fig. 8).

For $(\text{Eu}_3\text{O})\text{In}$ and $(\text{Eu}_3\text{O})\text{Sn}$ XAS spectroscopy at the Eu L_{III} edge indicates pure $\text{Eu}^{2+}(4f^7)$ states since the edges are shifted about $\Delta E = 10$ eV to lower energies as compared with those of Eu^{3+}F_3

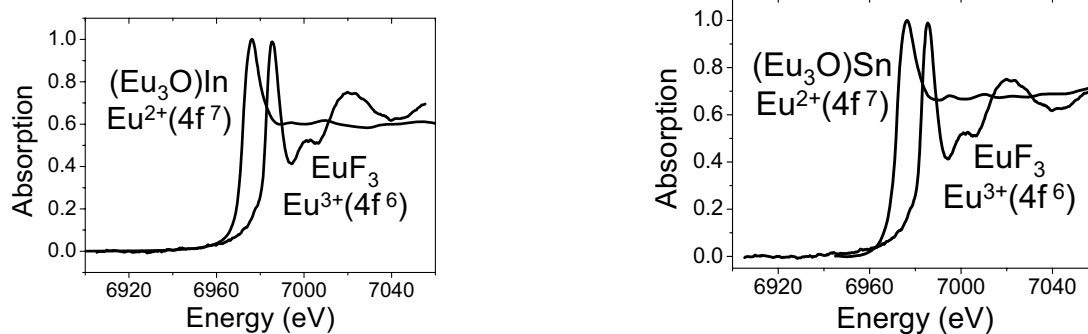


Fig. 9: XAS spectra of a) $(\text{Eu}_3\text{O})\text{In}$ and EuF_3 taken at the Eu L_{III} edge at ambient conditions and b) of $(\text{Eu}_3\text{O})\text{Sn}$ taken at the Eu L_{III} edge and the spectrum of EuF_3 taken simultaneously. The white line at lower energy is attributed to an $\text{Eu}^{2+}(4f^7)$ state, the signal at higher energies is assigned to an $\text{Eu}^{3+}(4f^6)$ state.

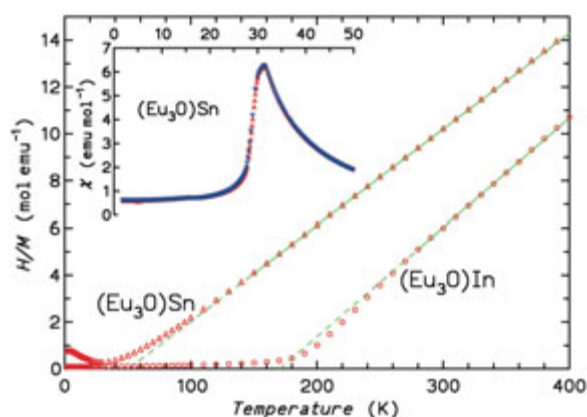


Fig. 8: Inverse magnetic susceptibility H/M of $(\text{Eu}_3\text{O})\text{In}$ and $(\text{Eu}_3\text{O})\text{Sn}$. The Curie-Weiss fits (continuous lines) and their extrapolations (dashed lines) are shown. The inset displays $\chi(T) = M/H$ of $(\text{Eu}_3\text{O})\text{Sn}$ for $H = 100$ Oe around the antiferromagnetic transition temperature.

(Fig. 9). No indication of any $\text{Eu}^{3+}(4f^6)$ contribution was observed. Measurements at temperatures below ambient down to $T = 20$ K did not indicate any change in the $\text{Eu}(4f)$ occupation.

The electrical resistivities $\rho(T)$ (Fig. 10) of both compounds are much larger than the typical maximum value of $100 \mu\Omega \text{ cm}$ for intermetallic compounds, however, the compounds still behave as metallic conductors. The magnetic ordering transitions of both compounds are marked by clear cusps. These effects are due to spin-disorder scattering which is expected to be very strong in Eu^{2+} compounds. An additional small cusp in $\rho(T)$ is observed for $(\text{Eu}_3\text{O})\text{Sn}$ at 89 K. Compared to the resistivity of $(\text{Eu}_3\text{O})\text{In}$ (after subtracting the magnetic contributions to both data sets) the resistivity of the Sn containing compound is about a factor of 3 – 4 higher. This fact may be related to metallic

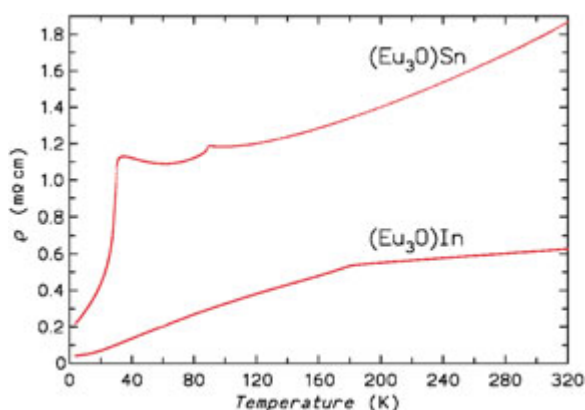


Fig. 10: Electrical resistivity $\rho(T)$ of the compounds $(Eu_3O)In$ and $(Eu_3O)Sn$

properties of $(Eu_3O)In$ (electron deficient like the related alkaline-earth metal compounds, in particular $(Ca_3N)Ti$ [23]) and the possibility to describe $(Eu_3O)Sn$ according to the octet rule: $(Eu^{2+})_3(O^{2-})(Sn^{4-})$. Therefore, in agreement with the physical properties measurements, $(Eu_3O)Sn$ may be classified as a heavily doped degenerated semiconductor or a semimetal. This might influence also the magnetic behavior of $(Eu_3O)In$ and $(Eu_3O)Sn$: Due to the presence of conduction electrons, the In compound may show larger ferromagnetic RKKY interactions between Eu species leading to ferromagnetic order at a high temperature T_C . Weaker RKKY interactions are present for $(Eu_3O)Sn$ in a semiconducting state. The positive $\Theta \approx 50$ K despite the antiferromagnetic order at $T_N = 31.4$ K indicates competing ferromagnetic and antiferromagnetic interactions with first and second shell Eu neighbors which are probably much smaller for the In compound.

Systems $(R_3N)Sn$ ($R = La - Sm$)

Formation and Crystal Structures

Experimentally, the cubic Perovskite nitrides $(La_3N)Sn$, $(Ce_3N)Sn$, $(Pr_3N)Sn$, $(Nd_3N)Sn$, and $(Sm_3N)Sn$ were obtained, while no such nitrides could be synthesized with $R = Sc, Gd, Lu$. Together with the report on $(Nd_3N)Sn$ from literature [18], this leads to the assumption that such nitrides do only form with the larger rare-earth metals with the border of existence located at Gd. The corresponding Perovskite carbides, for comparison, exist for all rare-earth metals R . Similar to the previous observations for the respective nitrides with In,

$(R_3N)In$ [2], the binary compounds Ce_3Sn and Pr_3Sn show high macroscopic hardness paired with some ductility, while introduction of nitrogen leads to brittle compounds.

Figure 1b plots the cubic root of the volumes per formula unit, $(V_0)^{1/3}$, for the compounds $(R_3Z)Sn$ with $Z = \square, C, N, O$ as a function of the ionic radii of the rare-earth metal ions in the oxidation state +3 ($CN = 6$) [13 – 16, 18, 24, 25, 33 – 35, 39]. The unit cell of Ce_3Sn significantly deviates from those of La_3Sn and Pr_3Sn to a smaller value, while the magnetic moment of $\mu_{eff}/Ce\text{-atom} = 2.2 \mu_B$ is only slightly reduced (expected value for $Ce^{3+}(4f^1)$: $\mu_{eff}/Ce\text{-atom} \approx 2.5 \mu_B$) [36]. This deviation of the unit cell dimension to smaller values than expected from those of the other compounds R_3Sn was discussed to arise from substitutional disorder [17]. As can be taken from Figure 1b the unit cells of the carbides with $R = La, Pr$ are only slightly larger than those reported for the binary compounds. The value for $(Yb_3C)Sn$ clearly deviates from the monotonic behavior to a larger value which might be interpreted as indication for a $Yb^{2+}(4f^{14})$ contribution. This view is supported by data on $(Yb_3O)Sn$ [24], where the cubic unit cell parameter indicates the presence of $Yb^{2+}(4f^{14})$. The cubic unit cell of the only previously known nitride $(Nd_3N)Sn$ is even larger than that of $(Nd_3C)Sn$ [18].

The obtained values for the cubic unit cell parameters of the nitrides (Fig. 1b) are well in correspondence with each other, the previously reported volume of $(Nd_3N)Sn$ [18] strongly deviating towards a larger volume. This observation, together with the fact that the volume of the nitride is even larger than that of the corresponding carbide, may fuel speculations on a homogeneity range towards higher Sn contents. Striking are the smaller unit cell parameters of $(La_3N)Sn$ and $(Pr_3N)Sn$ compared with those of the respective binary compounds, similar to what was observed for $(Sc_3N)In$ compared to Sc_3In . For the Sn containing phases this fact cannot be related to different structure motifs of the metal constituents, as was discussed for the respective In systems [2].

Magnetic and Electronic Properties

As might be expected $(La_3N)Sn$ shows a weak, nearly temperature-independent paramagnetism of the order of magnitude of a Pauli-paramagnet ($\chi_0 = +133 \times 10^{-6}$ emu/mol). Superconductivity at $T_c = 5.8$ K is evidenced in magnetization measurements

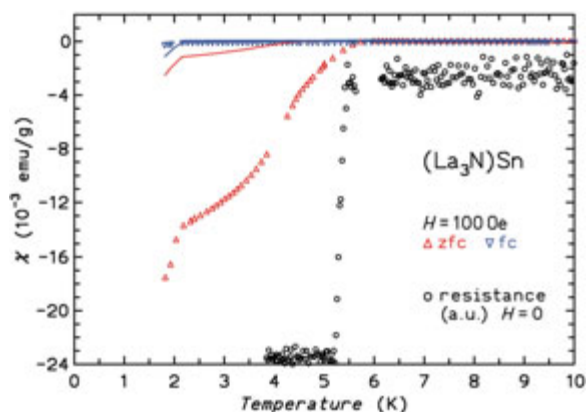


Fig. 11: $(\text{La}_3\text{N})\text{Sn}$: Electrical resistance (black circles) and magnetic susceptibility of an as prepared sample. The observed superconductivity is most likely due to a thin La film (see main text).

recorded on microcrystalline pieces of $(\text{La}_3\text{N})\text{Sn}$ (Fig. 11, full shielding in zero field cooling, but small Meissner effect in field cooling). Remarkably, this value of T_c nearly coincides with the reported superconducting transition temperature of La_3Sn (Cu_3Au type structure) of $T_c = 6.2$ K [15]. The corresponding electrical resistivity as a function of temperature measured on a microcrystalline bar-shaped piece of $(\text{La}_3\text{N})\text{Sn}$ applying a current density of $J = 3$ mA/mm² indicates metallic behavior, but no superconductivity. The transition to a superconducting state in resistivity measurements was only observed using a current density as low as $J = 0.75$ mA/mm². This gives rise to two possible interpretations: i) $(\text{La}_3\text{N})\text{Sn}$ is a superconductor with a rather small critical current density, or ii) all grains of the sample are covered with a thin layer of a superconducting second phase not visible in XRD (e.g., elemental La, $T_c(\beta\text{-La}) = 5.9$ K [38]). A second magnetization measurement on the identical material after grinding to a fine powder revealed only rudimentary remains of the shielding signal – a strong support for the second interpretation.

$(\text{Ce}_3\text{N})\text{Sn}$ orders antiferromagnetically at $T_N = 6.8(2)$ K. Deviations from linear Curie-Weiss behavior at higher temperatures are due to crystal field effects. The effective magnetic moment was determined to $\mu_{\text{eff}}/\text{Ce} = 2.46 \mu_B$, well in correspondence to the expected value of $\mu_{\text{eff}} = 2.54 \mu_B$ for the free $\text{Ce}^{3+}(4f^1)$ ion.

The magnetic properties of $(\text{Pr}_3\text{N})\text{Sn}$ are quantitatively similar to the respective In phase [2]. The effective magnetic moment $\mu_{\text{eff}}/\text{Pr-atom} = 3.70 \mu_B$ is consistent with a $\text{Pr}^{3+}(4f^2)$ state. The antiferromagnetic ordering takes place at $T_N = 48(1)$ K, again at a considerably higher temperature than for the corresponding In containing phase.

Conclusions

The binary phases La_3Al and Ce_3Al apparently do not exist in a stable cubic Cu_3Au type modification at ambient pressure. Reports are likely due to unnoticed impurities and formation of cubic Perovskites $(R_3Z)\text{Al}$ ($Z = \text{O}, \text{N}, \text{C}$). The ternary nitrides and oxides tolerate only small Z deficiencies. The carbide with $R = \text{Ce}$ apparently exhibits intrinsic carbon deficiency, resulting in a smaller unit cell as compared to the Perovskite carbides of other rare-earth metals. Large homogeneity ranges in the sense of solid solutions between the respective ternary oxide, nitride and carbide of the same rare-earth metal are apparent.

In all compounds discussed, Ce is present in a $\text{Ce}^{3+}(4f^1)$ electronic state, and Eu in a $\text{Eu}^{2+}(4f^7)$ state. The Ce moments order antiferromagnetically with T_N roughly decreasing and scaling with increasing unit cell dimension of the compounds, i.e., with increasing distance $d(\text{Ce}-\text{Ce})$. $(\text{Eu}_3\text{O})\text{Sn}$, which can be described by exclusively containing closed shell ions, probably exhibits semiconducting properties. An electronic imbalance by exchange of Sn by In leads to metallic properties and different magnetic order phenomena. A similar effect of exchange of Eu by trivalent rare-earth metal species is observed in compounds $(R_3\text{N})\text{Sn}$.

Electronic band structure calculations performed for the lanthanum compounds with compositions $(\text{La}_3Z)\text{Al}$ reveal a trend towards increased mixing of Z and La states on going from O via N to C. Formation of a band gap even in the formally electronically balanced $(\text{La}_3\text{C})\text{Al}$ is mainly prohibited by insufficient charge transfer between the metal species and corresponding La–La bonding. Investigations of the magnetic properties display interesting phenomena (e.g. metamagnetism) which are an attractive topic for their own.

References

- [1] M. Kirchner, R. Niewa, W. Schnelle, F. R. Wagner and R. Kniep, Max-Planck-Institut für Chemische Physik fester Stoffe, Scientific Report 2001/2002, Dresden, January 2003.
- [2] M. Kirchner, W. Schnelle, F. R. Wagner and R. Niewa, *Solid State Sci.* **5** (2003) 1247.
- [3] T. Dagerhamn, *Arkiv Kemi* **27** (1967) 363.
- [4] A. Saccone, A. M. Cardinale, S. Delfino and R. Ferro, *Z. Metallkd.* **87** (1996) 82.
- [5] J. H. N. van Vucht, *Z. Metallkd.* **48** (1957) 253.
- [6] K. H. J. Buschow and J. H. N. van Vucht, *Z. Metallkd.* **57** (1966) 162.
- [7] K. H. J. Buschow, *J. Less-Common Met.* **9** (1965) 452.
- [8] J. C. Schuster, *J. Less-Common Met.* **105** (1985) 327.
- [9] A. Leineweber and H. Jacobs, *J. Alloys Comp.* **278** (1998) L10.
- [10] A. Iandelli, National Physical Laboratory, United Kingdom, **1** (1958) 3F-2-3F-11.
- [11] J. Sakurai, Y. Murashita, Y. Aoki, T. Fujita, T. Takabatake and H. Fujii, *J. Phys. Soc. Jpn.* **58** (1989) 4078.
- [12] K. H. Mader and W. E. Wallace, *J. Less-Common Met.* **16** (1968) 85.
- [13] W. Jeitschko, H. Nowotny and F. Benesovsky, *Monatsh. Chem.* **95** (1964) 1040.
- [14] H. Haschke, H. Nowotny and F. Benesovsky, *Monatsh. Chem.* **97** (1966) 1045.
- [15] C. S. Garde, J. Ray and G. J. Chandra, *Alloys Comp.* **198** (1993) 165.
- [16] T. M. Gesing, K. H. Wachtmann and W. Jeitschko, *Z. Naturforsch.* **52b** (1997) 176.
- [17] M. Kirchner, F. Gäbler, W. Schnelle, F. R. Wagner and R. Niewa, *Z. Kristallogr.* in press.
- [18] H. Haschke, H. Nowotny and F. Benesovsky, *Monatsh. Chem.* **98** (1967) 2157.
- [19] J.-T. Zhao, Z.-C. Dong, J. T. Vaughan, J. E. Ostenson and J. D. Corbett, *J. Alloys Comp.* **230** (1995) 1.
- [20] M. Y. Chern, D. A. Venno and F. J. DiSalvo, *J. Solid State Chem.* **96** (1992) 415.
- [21] F. Gäbler, M. Kirchner, W. Schnelle, U. Schwarz, M. Schmitt, H. Rosner and R. Niewa, *Z. Anorg. Allg. Chem.* **630** (2004) 2292.
- [22] F. Gäbler, M. Kirchner, W. Schnelle, M. Schmitt, H. Rosner and R. Niewa, *Z. Anorg. Allg. Chem.* **631** (2005) 397.
- [23] R. Niewa, W. Schnelle and F. R. Wagner, *Z. Anorg. Allg. Chem.* **627** (2001) 365.
- [24] A. Velden and M. Jansen, *Z. Anorg. Allg. Chem.* **630** (2004) 234.
- [25] R. Türck, Ph D Thesis, Universität Stuttgart, Germany, 1996.
- [26] R. Niewa, D. A. Zherebtsov, M. Kirchner, M. Schmidt and W. Schnelle, *Chem. Mater.* **16** (2004) 5445.
- [27] U. Zachwieja and H. Jacobs, *J. Less-Common Met.* **161** (1990) 175.
- [28] M. Morinaga, K. Sato, J. Harada, H. Adachi, S. Ohba and Y. Sato, *J. Phys. C.: Solid State Phys.* **16** (1983) L177.
- [29] J.-E. Jørgensen, J. D. Jørgensen, B. Batlogg, J. P. Remeika and J. D. Axe, *Phys. Rev.* **B33** (1986) 4793.
- [30] M. Y. Chern, F. J. DiSalvo, J. B. Parise and J. A. Goldstone, *J. Solid State Chem.* **96** (1992) 426.
- [31] B. Huang, J. D. Corbett, *Z. Anorg. Allg. Chem.* **624** (1998) 1787.
- [32] K. H. J. Buschow and J. H. N. van Vucht, *Philips Res. Rep.* **22** (1967) 233.
- [33] H. Haschke, H. Nowotny and F. Benesovsky, *Monatsh. Chem.* **97** (1966) 716.
- [34] H. Hollek, *J. Less-Common Met.* **52** (1977) 167.
- [35] H. Haschke, H. Nowotny and F. Benesovsky, *Monatsh. Chem.* **97** (1966) 1469.
- [36] F. Weitzer, K. Hiebl and P. Rogl, *J. Less-Common Met.* **175** (1991) 331.
- [37] I. J. McCollm, N. J. Clark and B. Mortimer, *J. Inorg. Nucl. Chem.* **33** (1971) 49.
- [38] A. L. Griorgi, E. G. Szklarz, M. C. Krupta and N. H. Krikorian, *J. Less-Common Met.* **17** (1969) 121.
- [39] M. Kirchner, W. Schnelle and R. Niewa, *Z. Anorg. Allg. Chem.* in press.

¹ Present address: TU München, München, Germany